PASJ: Publ. Astron. Soc. Japan **61**, 1197–1209, 2009 December 25

Multifrequency Study of Giant Radio Pulses from the Crab Pulsar with the K5 VLBI Recording Terminal

Mikhail POPOV,[1] Vladimir SOGLASNOV,[1] Vladislav KONDRATIEV,[1,2,3] Anna BILOUS,[1,4] Olga MOSHKINA,[1,4]
Vasily ORESHKO,[5] Yury ILYASOV,[5] Mamoru SEKIDO,[6] and Tetsuro KONDO[6]
[1]*Astro Space Center of Lebedev Physical Institute, Leninsky Prospect 53, Moscow 117924, Russia*
mpopov@asc.rssi.ru, vsoglasn@asc.rssi.ru
[2]*West Virginia University, Department of Physics, Morgantown, WV 26506-6315, USA*
[3]*National Radio Astronomy Observatory, 520 Edgemont Road, Charlottesville, VA 22903-2475, USA*
vlad.kondratiev@gmail.com
[4]*Moscow Institute of Physics and Technology, 141700, 9, Institutskii per., Dolgoprudny, Moscow, Russia*
hanna.bilous@gmail.com, MoshkinaOlga@yandex.ru
[5]*Puschino Radio Astronomical Observatory, Astro Space Center, Lebedev Physical Institute,*
Pushchino, Moscow Reg., 142292, Russia
oreshko@prao.ru, ilyasov@prao.ru
[6]*Kashima Space Research Center, National Institute of Information and Communications Technology,*
893-1, Hirai, Kashima, Ibaraki 314-8501
sekido@nict.go.jp, kondo@nict.go.jp

(Received 2009 February 19; accepted 2009 July 9)

Abstract

Simultaneous multifrequency observations of Crab pulsar giant pulses (GPs) were performed with the 64-m Kalyazin radio telescope at four frequency ($\nu = 0.6$, 1.4, 2.2, and 8.3 GHz) using the K5 VLBI recording terminal. The K5 terminal provided continuous recording in 16×4-MHz wide frequency channels distributed over 4 frequency bands. Several thousand GPs were detected during about 6 hours of observations on two successive days in 2005 July. The radio spectra of single GPs were analyzed at separate frequencies and over the whole frequency range. These spectra manifest notable modulation over the frequency ranges, $\Delta\nu$, both on large ($\Delta\nu/\nu \approx 0.5$) and small ($\Delta\nu/\nu \approx 0.01$) frequency scales. A cross-correlation analysis of GPs at 2.2 GHz showed that their pulse shapes can be interpreted as being an ensemble of unresolved bursts grouped together on time scales of $\approx 1\,\mu$s, being well-correlated over a 60-MHz band. The corresponding GP cross-correlation functions do not obey the predictions of the amplitude-modulated noise model of Rickett (1975), thus indicating that unresolved components represent a small number of elementary emitters.

Key words: Pulsars — giant pulses, Crab pulsar, PSR B0531+21 — e-VLBI terminal K5

1. Introduction

Giant pulses (GPs) represent an extraordinary phenomenon in pulsar radio emission. First, they have huge peak flux densities, that may be as great as several millions of janskys (Cordes et al. 2004; Soglasnov 2007). Second, their duration is ultra short with the GP fundamental components being even shorter than 2 ns (Hankins et al. 2003; Hankins & Eilek 2007). Third, these elementary nanopulses are strikingly almost completely circularly polarized, either left- or right-handed (Cognard et al. 1996; Popov et al. 2004; Hankins et al. 2003). Giant pulses are reliably known only from seven pulsars (see, e.g., Knight 2006, and references therein), but the properties of GPs were studied extensively only for two objects: for the original millisecond pulsar B1937+21 (Cognard et al. 1996; Kinkhabwala & Thorsett 2000; Soglasnov et al. 2004; Kondratiev et al. 2007b), and for the Crab pulsar (see the most recent review by Bilous et al. 2008 and references therein). In contrast to regular radio pulses, which typically have a Gaussian distribution, the cumulative distribution of GP energies follows a power law $N(E > E_0) \propto E_0^{-\alpha}$ with the exponent α being in the range of 1.5–2.5 (Popov & Stappers 2007; Bhat et al. 2008). These authors also reported about the deviation from the single power-law fit of cumulative distributions at low energies. No deviations, however, were found at the highest energies, even during 160-hour monitoring of the Crab pulsar with the Kalyazin 64-m radio telescope at frequencies of 0.6, 1.65, and 4.85 GHz (Popov et al. 2008). These three-frequency observations demonstrated that the pulse energy, in general, grows with decreasing frequency, and the spectral index is of about -1.8. However, the radio spectra of individual giant pulses manifest deep modulations both on small and large frequency scales (Hankins & Eilek 2007; Popov & Stappers 2003; Popov et al. 2008). In this paper we present an analysis of results obtained from simultaneous 4-frequency observations of GPs from the Crab pulsar conducted with the 64-m Kalyazin radio telescope at frequencies of 0.6, 1.4, 2.2, and 8.3 GHz using the K5 VLBI recording terminal. A description of the observing setup and data reduction pipeline is given in sections 2 and 3. The results of our GP studies at different frequencies are reported in sections 4, 5, and 6, and the conclusions are given in section 7.

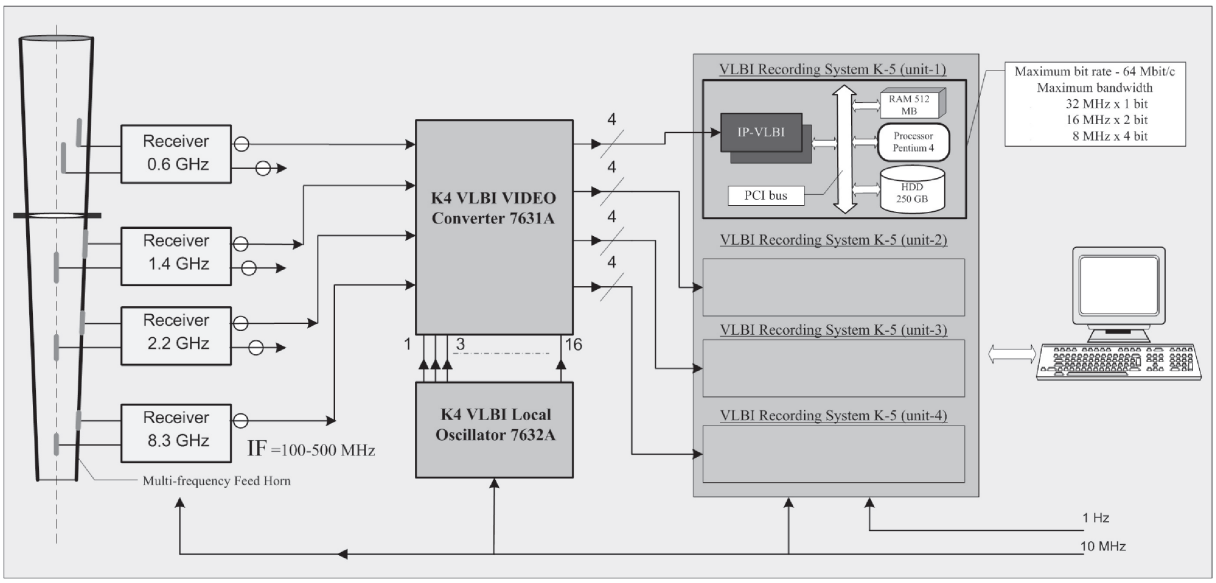

Fig. 1. Block diagram of the antenna feed line of the 64-m Kalyazin radio telescope with the K5/VSSP VLBI recording terminal.

Table 1. Observations summary.*

Band	Frequency channels (MHz)				SEFD	$\tau_{\rm DM}$	$N_{\rm p}$†	$S_{\rm max}$
	f_1	f_2	f_3	f_4	(Jy)	(μs)		(MJy)
600	599.6	–	–	–	1300	8500	$\sim$10000‡	2.2
1400	1395.0	1410.0	1425.0	1440.0	1150	650	1112	3.7
2200	2140.0	2160.0	2180.0	2200.0	1050	180	631	1.3
8300	8260.0	8280.0	8300.0	8320.0	240	3	1	0.04

* Columns list the frequency band, the frequency channels setup for every band with the values corresponding to the lower edge of the channel, f_1–f_4, the system equivalent flux density (SEFD) including the contribution from the Crab nebula (see text), the estimated dispersion smearing time in a single frequency channel ($\tau_{\rm DM}$), the total number of events found in a total band ($N_{\rm p}$), and the peak flux density of the strongest event ($S_{\rm max}$).

† Giant pulses can be simultaneously detected in more than one frequency channel, i.e., the actual number of unique pulses detected is smaller than the total number of events in all frequency channels, $N_{\rm p}$.

‡ See section 6 for explanation.

2. Observations

Multifrequency observations of the Crab pulsar were conducted on 2005 July 20–21 with the 64-m Kalyazin radio telescope simultaneously at four frequency bands: 0.6, 1.4, 2.2, and 8.3 GHz. The total observing time was about 6 hr. The simultaneity of observations at four frequencies was possible owing to the multifrequency feed with which the Kalyazin radio telescope is equipped. To record the data, we used a K5/VSSP VLBI recording terminal (Kondo et al. 2002) and a K4 baseband converter provided by the Kashima VLBI group of the National Institute of Information and Communications Technology (NICT, Japan) for joint VLBI observations of pulsars under mutual agreement. A block diagram of the antenna feed line with the K5/VSSP VLBI recording terminal is presented in figure 1. The terminal consists of 4 workstations with K5/VSSP PCI-bus boards, which allow us to record up to 16 channels, each with a bandwidth of 4 MHz. The channels may be distributed in frequencies and/or polarizations by using the K4 baseband converter. In our observations we used the frequency setup presented in table 1. The channel frequencies f_1–f_4 from the table correspond to the lower edge of each frequency channel, and only the upper subbands were recorded. At a frequency band of 600 MHz, only one 4-MHz channel was used, because of limitations by radio-frequency interference. In all other bands we used four channels distributed along the whole band, as indicated in table 1.

The system equivalent flux density (SEFD) for every band is dominated by the contribution from the Crab nebula, which is given in table 1. The flux densities for the Crab nebula were calculated by using the relation $S_f = 955\,f^{-0.27}$, with f expressed in GHz (Cordes et al. 2004). At 8.3 GHz the solid angle of the radio telescope beam covers only 20% of the area occupied by the nebula. Thus, we estimated the contribution from the Crab nebula to be 5-times less at this frequency, assuming an uniform surface brightness distribution.

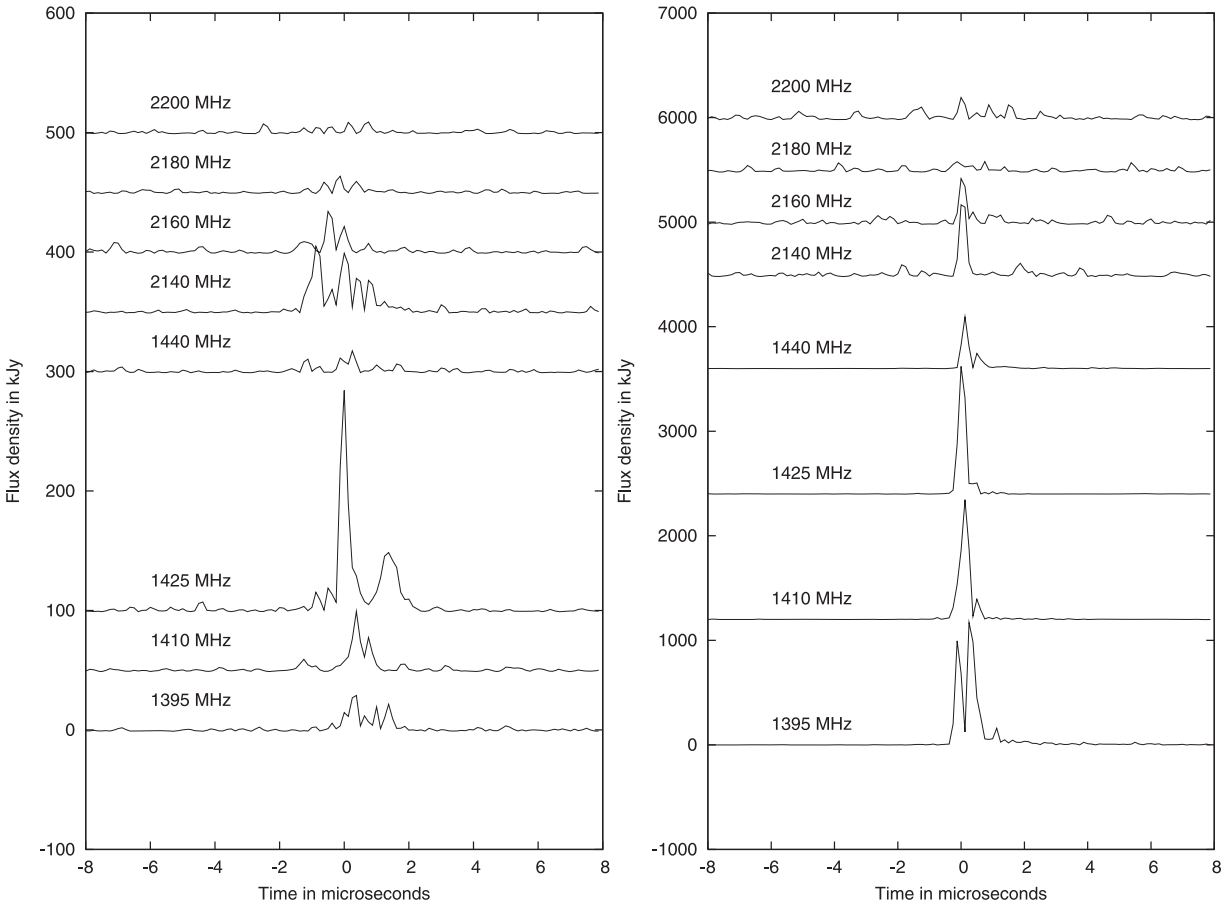

Fig. 2. Example of strong giant pulses detected simultaneously at 1.4 and 2.2 GHz in several frequency channels. The zero value in time corresponds to a sample with the maximum flux density of the giant pulse in any of the channels.

3. Data Reduction

The core of the processing pipeline consisted of successive decoding of the data as well as corrections for bit-statistics and dedispersion. Every single frequency channel was decoded according to the K5/VSSP (IP-VLBI) Board Data format[1] so as to produce a raw binary data stream. The decoded data represented the stream of only four alternating numbers: -3, -1, $+1$, and $+3$, according to the VLBA coding of 2-bit digitized values. These data were then corrected for the bit-statistics, i.e., the decoded values were adjusted to real ones that correspond to instantaneous $\pm 1\,\sigma$ brightness levels by using a technique developed by Jenet and Anderson (1998). To coherently dedisperse the data we used a predetection dispersion removal technique pioneered by Hankins (1971; see also Hankins & Rickett 1975). More details about the correction for bit-statistics and coherent dedispersion can be found in Popov et al. (2002). However, for the coherent dedispersion, unlike equation 1 from Popov et al. (2002), we have used exact equations for the phase correction:

$$\delta\phi(f) = \frac{2\pi \mathrm{DM}}{Df}\left(\frac{\Delta f}{f_0}\right)^2, \qquad (1)$$

where DM is the dispersion measure in pc cm^{-3}, $D = 2.41 \times 10^{-16}$ pc cm^{-3} s the dispersion constant, f_0 the lowest frequency of the frequency channel, f the current frequency, and $\Delta f = f - f_0$.

To allow for a direct comparison of the times of arrival (TOA) of giant pulses, we reduced the TOAs in all frequency channels within a band to the highest frequency (except for the data at 0.6 GHz where we had only one frequency channel). This was done by introducing a time delay via a linear phase correction, k_f, in the corresponding spectra simultaneously with a correction for $\delta\phi(f)$; k_f is given by $k_f = 2\pi \times dt/N$, where dt is the time delay between the corresponding frequencies in samples (including fractional part), and N is equal to the number of samples in the array used for the Fast Fourier Transform (FFT). We used $N = 2097152$, corresponding to a time interval of 262.144 ms, and covering about 7.8 periods of the Crab pulsar. The dedispersion correction of every such chunk of data resulted in a number of spoiled samples in the restored signal due to the cycle nature of the convolution made through the FFT. The duration of this spoiled portion is equal to the dispersion time in a single frequency channel, τ_{DM}, of which the estimated approximate values are given in table 1. To reconstruct the signal without gaps, the successive chunks of data were overlapped by τ_{DM}. The used value of DM $=$ 56.738 cm^{-3} pc was taken from the Jodrell Bank Crab Pulsar

[1] ⟨http://www2.nict.go.jp/w/w114/stsi/K5/VSSP/data_format_e.pdf⟩.

Monthly Ephemeris[2] (Lyne et al. 1993) for the epoch close to our observations.

To search for GPs at all frequencies, except 600 MHz[3], we set up the detection threshold at a level of $20\,\sigma$ above the mean value for the signal with the original sample time of 125 ns. The statistics of amplitudes x of such a signal is close to a χ^2-distribution with 2 degrees of freedom $P(x > a) = \exp(-a)$, where P is the probability of the amplitude x of the signal exceeding the threshold a, and a is in units of σ. Thus, the probability of false detection with a threshold of of $20\,\sigma$ above the mean level is 7.6×10^{-10}, and for a sampling rate of 8 MHz it will lead to the detection of one false GP in every 3 min. During a subsequent analysis, only events that occurred in the narrow windows located at the longitudes of the main pulse and the interpulse were selected. These windows were each about $100\,\mu$s wide and occupied only 0.6% of the period. Therefore, false detection occurred only once per several hours.

The total numbers of detected events were about 10000, 2700, 1600, and 1 at frequencies of 0.6, 1.4, 2.2, and 8.3 GHz, respectively (see table 1). At 1.4 and 2.2 GHz, sufficiently strong GPs were detected simultaneously in several frequency channels, and the number of real GPs was 2–3 times less than the total number of detections. The brightest GP was found at 1.4 GHz with a peak flux density of 3.7 MJy. Examples of strong giant pulses detected simultaneously at 1.4 and 2.2 GHz are shown in figure 2.

4. Giant Pulse at 8.3 GHz

Only one giant pulse was detected at the observing frequency of 8.3 GHz at a level of 30σ with a peak flux density of about 10 kJy, nearly equal in all four frequency channels. The pulse profile is shown in figure 3. The event was not accompanied by notable emission at any of the lower frequency ranges, thus proving $\Delta\nu/\nu \leq 0.5$ for the radio spectrum of this pulse. On the other hand, at 8.3 GHz the pulse flux density was constant over about 80 MHz. The only detection did not allow us to perform a statistical analysis of the GP shapes, widths, and energies, as we did for other frequencies (see below). High-frequency observations of giant pulses from the Crab pulsar were recently carried out by some of us with the 100-m Effelsberg radio telescope at 8.7, 15.1, and 22.2 GHz. The first results from the ultra-high time-resolution data obtained with the Tektronix oscilloscope were reported by Jessner et al. (2008).

5. Giant Pulses at 1.4 and 2.2 GHz

Unlike the high frequency of 8.3 GHz, where only one GP was detected, we found 1112 and 631 GP events in all four frequency channels at frequency bands of 1.4 and 2.2 GHz, respectively (see table 1). Below we present a statistical analysis of the GP energies and widths, and a study of the radio spectra, shapes, and DM variation.

[2] ⟨http://www.jb.man.ac.uk/~pulsar/crab.html⟩.

[3] At 600 MHz we did not selected individual GPs (except for the preliminary search). Instead of this, we compared the overall statistical properties of signal on emission longitude windows with those on the noise.

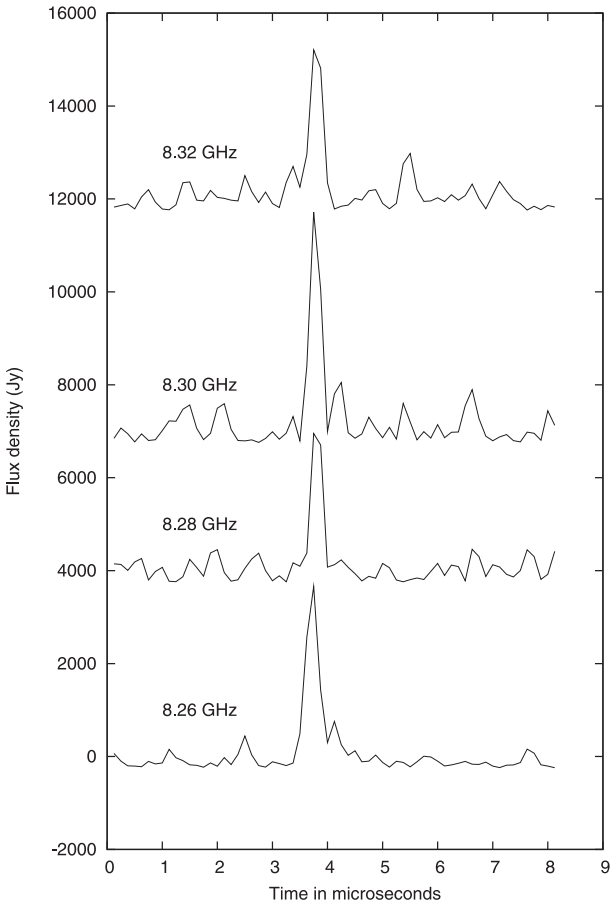

Fig. 3. Giant pulse detected at 8.3 GHz.

5.1. GP Width and Energy

Giant pulses vary significantly in their intensity and width, and show a broad variety in their shapes, as can be seen in figure 2. Therefore, it is rather difficult to compose an automated routine for GP's shape analysis. In this paper we propose two different techniques for such an analysis: the first one is based on a calculation of the integrated flux density over varying time boxes in the vicinity of a given GP (this subsection); the other method uses the analysis of any signal variance (see sub-subsection 6.1.1). Let us define the total width of a giant pulse ($w_{\rm tot}$) as a time interval Δt covering the vicinity of the GP that contains 90% of the total integrated flux density of a given GP. We calculate the integrated flux density (or pulse energy) as $E = \delta t[\sum_{i=0}^{n}(S_i - \langle S\rangle)]$, where δt is the sampling time (in our case $\delta t = 0.125\,\mu$s), and S_i are individual counts of the reconstructed flux density. To exclude any noise contribution, and to calculate the "net" on-pulse energy, one has to subtract the mean off-pulse flux density, $\langle S\rangle$, computed for the off-pulse window from the flux density value for every sample in the on-pulse window where the required energy is calculated. In this paper we express the pulse energy in units of kJy μs. Following these definitions, we calculated, first, the maximum value for the required pulse energy separated into two components: E_0^+ and E_0^- as $E_0^+ = \delta t[\sum_{i=0}^{n}(S_{\max+i} - \langle S\rangle)]$ and $E_0^- = \delta t[\sum_{i=0}^{n}(S_{\max-i} - \langle S\rangle)]$. These quantities were calculated in the vicinity of a point of maximum

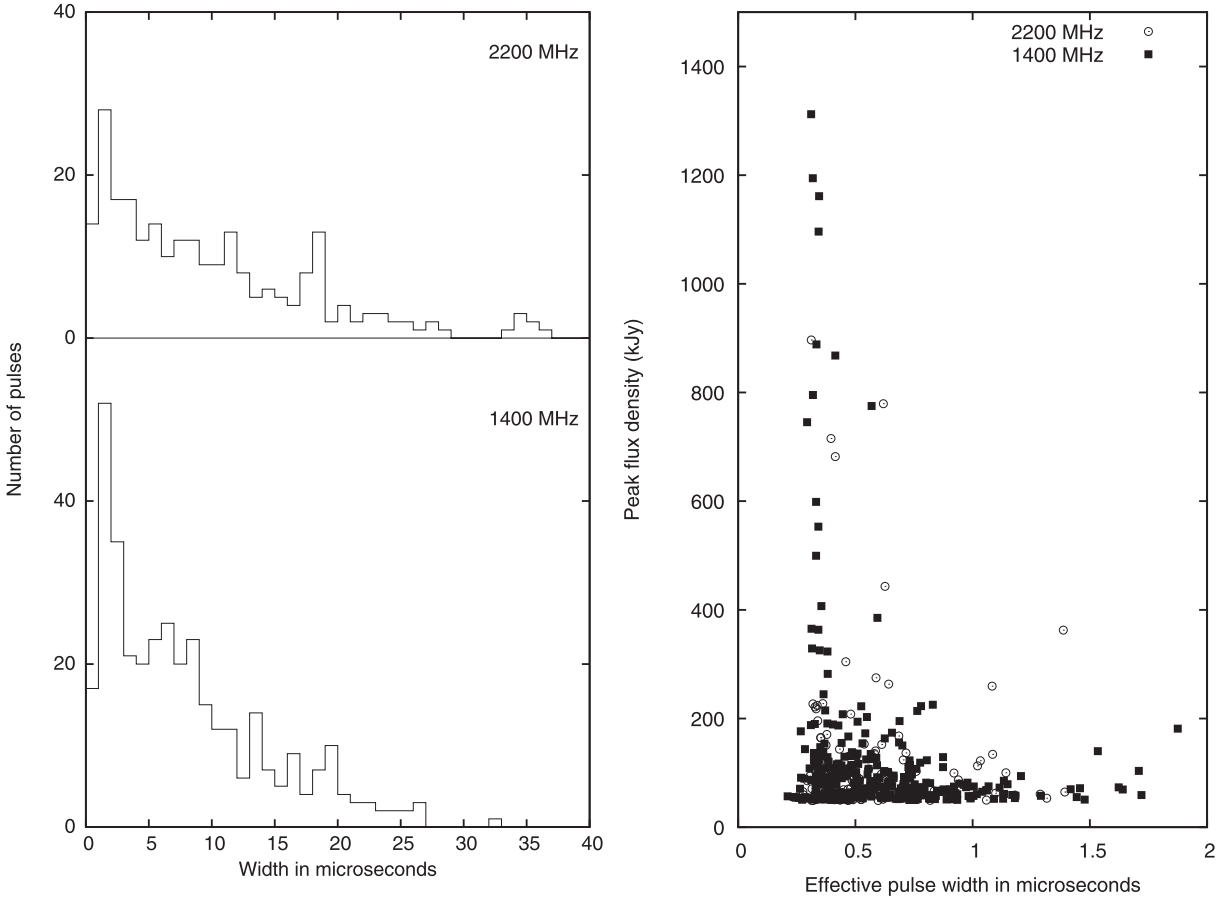

Fig. 4. Distribution of the total GP width $w_{\rm tot}$ (left), and the dependence between the peak flux density, $S_{\rm max}$, and the effective GP width, $w_{\rm e}$ (right), at 1.4 and 2.2 GHz.

flux density of a GP $S_{\rm max}$ over n samples in positive and negative time directions. We used $n = 256$, corresponding to the maximum expected pulse width of $\Delta t = 2n\delta t = 64\,\mu$s. E_0^+ and E_0^- may differ notably, since the pulse shape may not be symmetrical relative to its maximum. With E_0^+ and E_0^- in hand, we calculated trial values, $E_k^+ = \delta t[\sum_{i=0}^{k}(S_{\max+i} - \langle S\rangle)]$, and $E_k^- = \delta t[\sum_{i=0}^{k}(S_{\max-i} - \langle S\rangle)]$, for every step k in the organized loop from $k = 0$ to n. On every step k we compared the value of E_0^+ with the trial value of E_k^+, and the value of E_0^- with the trial value of E_k^-. When the corresponding difference, $|E_0^\pm - E_k^\pm|$, was less than $0.1\,E_0^\pm$, then the loop was terminated and the corresponding time t^+ or t^- was determined as the edge of a GP. Thus, the total GP width, $w_{\rm tot}$, was defined as $w_{\rm tot} = t^+ - t^-$. Correspondingly, the GP energy, $E_{\rm p}$, was defined as $E_{\rm p} = E_k^+ + E_k^-$, and the effective width of GP as $w_{\rm e} = E_{\rm p}/S_{\rm max}$. The term $w_{\rm e}$ is traditionally used in pulsar research; it describes the time interval where most of the pulse energy is concentrated, while $w_{\rm tot}$ corresponds to the whole pulse extent.

There is a strong constraint on the use of this approach to analyse a GP's shape. As already mentioned, the statistics of a detected signal in our case is close to a χ^2-distribution with two degrees of freedom. For such a signal, the root-mean-square deviation is equal to the mean value, i.e., the modulation index is equal to 1. Thus, the values of $E_k^\pm$ will manifest notable fluctuations. To keep these fluctuations reasonably small, one has to select only sufficiently strong pulses. We selected a threshold for the peak flux density for such pulses of $50\,\sigma$ for the estimated value for the maximum pulse width of $w_{\rm max} = 64\,\mu$s. Only 357 and 198 pulses met these requirements at 1.4 and 2.2 GHz, respectively.

Histograms of the total GP width, $w_{\rm tot}$, at 1.4 and 2.2 GHz are shown in figure 4 (left). Both the top and bottom histograms are skewed heavily towards shorter total widths. Note that only very strong GPs were analyzed; a weaker population of GPs may have a broader width distribution. The right histogram in figure 4 represents the dependency between the maximum flux density, $S_{\rm max}$, and the effective pulse width, $w_{\rm e}$, of a GP. It is clear that the strongest pulses tend to have shorter durations. The same tendency was found by Popov and Stappers (2007) at a frequency of 1.2 GHz on much broader statistics. We did not analyze the cumulative distributions at 1.4 and 2.2 GHz because of rather poor statistics as compared with the data used by Popov and Stappers (2007), but we will present such an analysis for our data, obtained at 600 MHz in section 6.

5.2. *Instantaneous GP Radio Spectra*

Given the multifrequency observations with the characteristic frequency setup (see table 1), we were able to analyze

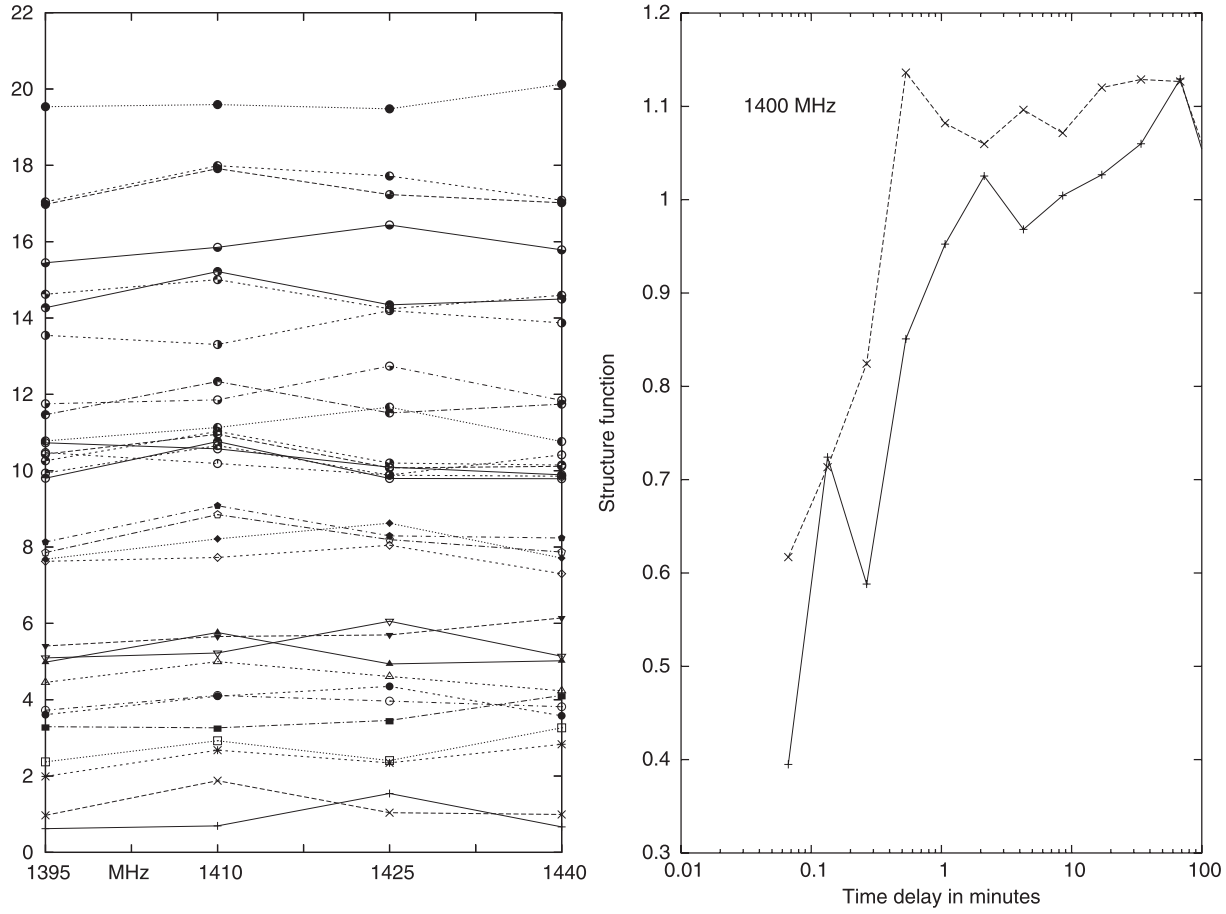

Fig. 5. Instant radio spectra of single GPs (left) and their structure functions of time variations for two successive observing days (right) at 1.4 GHz. Every curve connecting the same symbols in the left figure represent the form of an instant radio spectrum of a given GP. The location (shift) of a given spectrum at the ordinate axis corresponds to the arrival time of the GP expressed in minutes from the beginning of the observing set.

instantaneous radio spectra of detected strong GPs both over large and short frequency scales. It is important to take into account the effect of interstellar scintillation when measuring the integrated flux density of a giant pulse in a given receiver band. For this we considered the results of another experiment that was carried out by some of us over the course of our observations. This experiment was two-station VLBI observations between the 64-m Kalyazin radio telescope and 43-m Algonquine radio telescope (Canada) at 2244 MHz using the S2 recording system in a 16-MHz band (Kondratiev et al. 2007a). In the cross-correlation functions (CCF) of radio spectra of GPs detected at two stations, two frequency scales of diffraction modulation of the spectrum at 2244 MHz were found to be 50 and 450 kHz with equal modulation indices (Kondratiev et al. 2007a). Cordes et al. (2004) found that in the presence of interstellar scintillation the integrated flux density over the receiver band B will be subject to random fluctuations that follow a χ^2-distribution with $0.4B/\Delta\nu_{\rm d}$ degrees of freedom, where $\Delta\nu_{\rm d}$ is the decorrelation bandwidth. In the case of $\Delta\nu_{\rm d} > 0.2B$ the measured integrated flux density is fully modulated by diffractive interstellar scintillation. For VLBI observations having $\Delta\nu_{\rm d} = 450$ kHz at 2.2 GHz and $B = 4$ MHz, $\Delta\nu_{\rm d} > 0.1B$ and the modulation of measured integrated flux densities will still be very significant. Following the steep power-law frequency dependence of the decorrelation bandwidth, $\Delta\nu_{\rm d}$, $\Delta\nu_{\rm d} \sim \nu^{4.4}$, for the Kolmogorov spectrum of electron-density irregularities (see, e.g., Lorimer & Kramer 2004), at a frequency of 1.4 GHz, $\Delta\nu_{\rm d}$ will be about 5-times less than at 2.2 GHz, and the scintillation modulations will be considerably smoothed. Therefore, we analyzed the properties of instantaneous GP radio spectra at short frequency scales only for the frequency band of 1.4 GHz.

The left plot in figure 5 shows an example of instantaneous GP radio spectra over 20 min of observations at 1.4 GHz. Points presented by the same symbols and connected with the same type of a line represent the pulse energy measured for a given GP and expressed in arbitrary units, but with the same scale for every curve. Each curve is placed at the ordinate axis in rough correspondance with the arrival time of a given GP. The arrival time is expressed in minutes from the beginning of a selected observing interval. The whole figure corresponds to one continuous observing set. The variations of the presented radio spectra with time seem to be random, but one can see that around the 10th minute of observations there are four GP spectra similar in appearance. This fact means that interstellar scintillation still affects the measurements. To make a quantitative analysis we calculated a structure function, $C^2(\tau)$, of the time variations of the instantaneous GP. A structure function is

traditionally used to classify time variations of some quantity, $Z(t)$, being investigated. For such a case, $C^2(\tau) = \frac{1}{N}\sum_{i=1}^{N}(Z_i - Z_{i+\tau})^2$. Then, $C^2(\tau) = 0$ with $\tau = 0$, and $C^2(\tau) = \sigma^2$ for $\tau > t$ with t indicating a characteristic time of the variability of $Z(t)$. Here, we transform the definition of $C^2(\tau)$ to apply it for the analysis of time variations of 4-point instantaneous spectra, Y_i^f, as $C^2(\tau) = \frac{1}{M}\sum_{i=1}^{N}\sum_{f=1}^{4}(Y_i^f - Y_{i+\tau}^f)^2$. Here, M is the number of combinations of radio GP spectra obtained within a given interval of time delay, τ; N is the total number of GPs in this test; and f = 1–4 corresponds to one of the four frequency channels listed in table 1. The calculated structure functions, $C^2(\tau)$, for two successive observing days are shown in the right plot of figure 5. It is evident that the structure functions become saturated at time intervals greater than one minute, and decreased rapidly at shorter time delays. Thus, we did observe the effect of interstellar scintillation at 1.4 GHz, which affects our measurements of radio GP spectra. Nevertheless, even at the shortest time delay (less than 10 s) between instantaneous GP spectra, the structure functions still have a notable value of about 0.5, which can be due to an intrinsic modulation of the GP spectra at a short frequency scale of $\Delta\nu/\nu \approx 0.01$.

Examples of instantaneous radio spectra in the frequency range 0.6–2.2 GHz for several GPs are presented in figure 6.

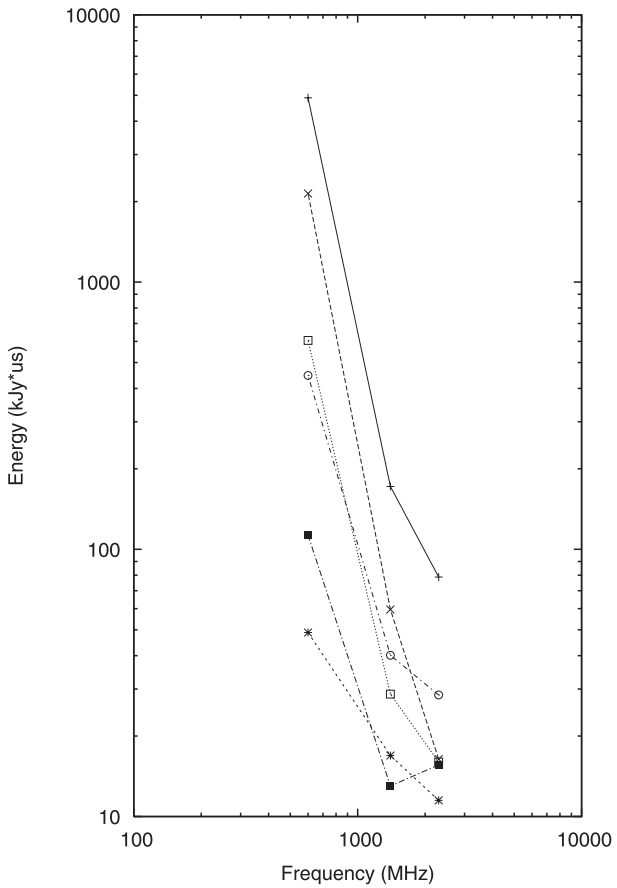

Fig. 6. Instantaneous radio spectra of single GPs in the frequency range of 0.6–2.2 GHz. Every polygonal line connecting the same symbols represents the spectrum of a selected giant pulse.

Every polygonal line connecting the same symbols represents the spectrum of a selected giant pulse. GP energies at 1.4 and 2.2 GHz were averaged over four frequency channels. There were only 27 strong GPs that occurred at all three observing frequencies of 0.6, 1.4, and 2.2 GHz. The mean spectral index, α, is equal to -2.6 and -1.8 for 0.6–1.4 GHz and 1.4–2.2 GHz, respectively.[4] Though our estimates are based on poor statistics of GPs, the tendency for the spectral index, α, to flatten at higher frequencies is doubtlessly apparent. The same behavior was reported by Popov et al. (2008) for a frequency range of 600–1650–4850 MHz.

5.3. *DM Variations*

There are 952 GPs out of a total of 1112 GP events (or about 85%) found at 1.4 GHz, which were identified with the GPs detected at 600 MHz. Therefore, we used them to determine accurate values of DM by comparing their TOAs at two observing frequencies. The results are shown in figure 7.

The left plot of figure 7 represents the dependence of the measured value of DM of GPs versus their time of arrival. Hankins and Eilek (2007) pointed out that at high radio frequencies (above 4 GHz), the DM values of GPs occurring at the longitudes of the interpulse differ noticeably from the DM values of GPs from the longitude of the main pulse. It is clear that in our observations at lower frequencies of 0.6 and 1.4 GHz there is no difference between DMs for GPs from different longitudes (see figure 7, left). The right plot of figure 7 shows a histogram of the dispersion measures of GPs. One can notice that the DM distribution is likely to be bimodal, and can be well-fitted by two Gaussians with mean values of 56.7363 and 56.7373 pc cm^{-3}. The difference, $\Delta DM = 0.001 \pm 0.0001$, was estimated with good formal accuracy. The difference corresponds to a time shift of about 10 μs at the observing frequency of 600 MHz. As it follows from the left plot in figure 7, the splitting can not be attributed to GPs that occurred at different longitudes (MP and IP).

5.4. *GP Profile Shapes*

As will be shown below in subsection 6.3, during our observations the scattering contribution was small, which allowed us to perform an analysis of the intrinsic shapes of GPs detected at a frequency of 2.2 GHz. Indeed, the expected scattering time, $\tau_{\rm scat}$, at this frequency was $\lesssim$200 ns, as extrapolated from the $\tau_{\rm scat}$ at 600 MHz, which is less than our time resolution of 250 ns (doubled sampling interval).

To study the profiles of individual GPs at a frequency of 2.2 GHz we used the approach of calculating the autocorrelation functions (ACFs) of GP profiles, the technique traditionally used to study the properties of the microstructure in pulsar radio emission (Hankins 1972; Cordes & Hankins 1973; Cordes 1976b). However, to avoid a noise spike at a zero lag of the ACFs, which would mask the presence of any unresolved components in the GP profiles, we calculated the CCFs between the profiles of the same GP recorded in different frequency channels. The cross-correlation function, $R_{1,2}(\tau)$, between profiles $I_1(t)$ and $I_2(t)$ of the same GP detected in

[4] The spectral index α is defined here as $E_\nu \propto \nu^\alpha$, where E_ν is the integrated flux density at frequency ν.

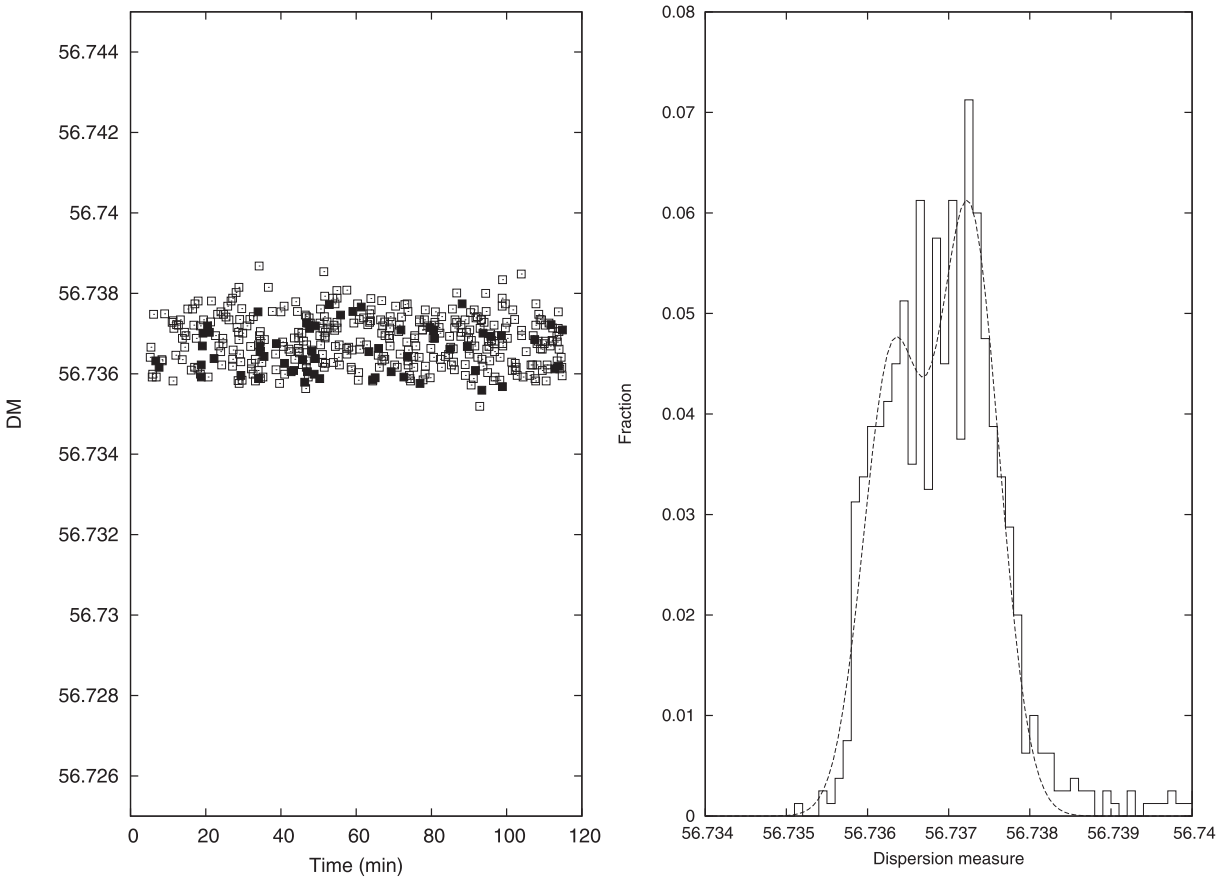

Fig. 7. Dispersion measure (DM) variations determined from times of arrival (TOA) of GPs at 600 and 1400 MHz. The left plot shows the measured DM values for different GPs versus the TOA of the giant pulse. Open squares show GPs that occurred at the longitude of the main pulse, while filled squares are those that occurred at the longitude of the interpulse. The right plot shows the histogram of DM variations. The dashed line is the two-Gaussian-component fit with the mean values of 56.7363 and 56.7373 pc cm^{-3}. This difference corresponds to the time shift of about 10 μs at 600 MHz.

two frequency channels is defined as

$$R_{1,2}(\tau) = [R_{1,1}(0)R_{2,2}(0)]^{-1/2} \sum_{t=1}^{N} I_1(t) I_2(t+\tau) \ , \qquad (2)$$

where t is the sample time within the GP, N is the total ON-pulse number of samples, and $I_1(t)$, $I_2(t)$ represent ON-pulse intensities with the OFF-pulse mean level subtracted. In our analysis we chose the duration of the ON-pulse window of 125 μs, or $N = 1000$ samples. For our 4 frequency channels at 2.2 GHz there are $C_4^2 = 6$ different frequency combinations listed in the first column of table 2.

Due to the effect of interstellar scintillation at this high frequency of 2.2 GHz, many GPs were not sufficiently strong in all frequency channels to provide a notable correlation coefficient for every pair of GP profiles. Thus, after the calculation of CCFs for all possible combinations of frequency channels for all 631 GP events found at 2.2 GHz, we chose only CCFs that have a sufficiently large value of the correlation coefficient at zero lag. For an ACF (or CCF), the root-mean-square deviation ($\sigma_{\rm acf}$) near zero lag is equal to $\sigma_{\rm acf} = 1/\sqrt{N}$. In our case for $N = 1000$, $\sigma_{\rm acf} \approx 0.03$, and for a subsequent analysis we selected only those CCFs with the correlation coefficient at zero lag larger than $8\,\sigma_{\rm acf} \approx 0.25$. There were 121 CCFs selected this way.

Table 2. Extra non-dispersive time delay δt.*

Frequency combination (MHz)	δt (μs)
2140–2160	-0.20 ± 0.04
2140–2180	-0.17 ± 0.04
2140–2200	-0.26 ± 0.07
2160–2180	0.05 ± 0.05
2160–2200	-0.06 ± 0.07
2180–2200	-0.01 ± 0.08

* Of the peak in the selected CCFs between GP profiles in different frequency channels. These delays represent the residual delays in time of arrival of GPs.

Figure 8 shows an example of selected CCFs calculated for one of the strong GPs. One can see a notable correlation between all frequency channels. There are two apparent time scales in the selected CCFs, namely a short one that occurred as a narrow feature that can be attributed to the presence of unresolved spikes in the GP structure, and an extended one with a duration of $\sim 1\,\mu$s. The majority of the selected CCFs had the same appearance. To study the extended time-scale

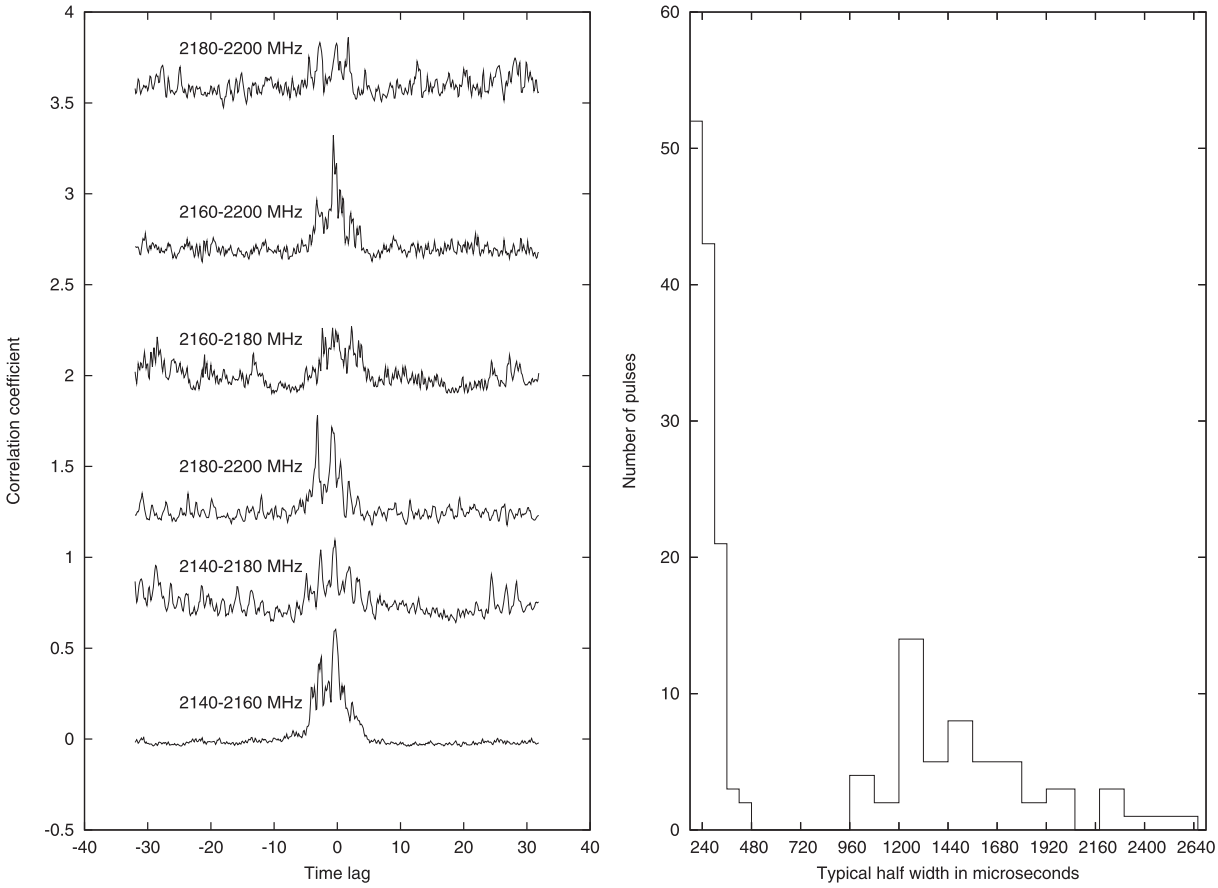

Fig. 8. Left hand side: Examples of cross-correlation functions (CCFs) between profiles in single frequency channels for one of the strong GPs at a frequency of 2.2 GHz. Right hand side: Histogram of the half-widths of the two time scales detected in the CCFs.

feature, we smoothed the CCFs over 20 samples, and selected only those with a correlation coefficient of 0.06 or larger at zero lag. Altogether, 102 of such CCFs were selected. The right plot of figure 8 shows the distribution of both time scales (short and extended) measured at the half-level of the maximum of the corresponding broad feature. There is a broad jitter of widths of the extended scales in the CCFs from about 1 μs up to more than 2 μs with a mean value of about 1.3–1.4 μs.

In addition to the measurements of the half-widths of the time scales detected in the CCFs, we also calculated the time delays of the CCF peaks relative to the expected value for DM = 56.738 pc cm^{-3}. The results are listed in table 2. One can see that apparent deviations (at a level of $> 3\,\sigma$) in GP times of arrival are present only for the frequency channel of 2140 MHz (the lowest frequency channel at 2.2 GHz). These deviations measured in a 60-MHz frequency range (2140–2200 MHz) at 2.2 GHz are much smaller than the residual dispersion delays of about 2 μs found in the arrival times of micropulses for the pulsars B0950+08 and B1133+16 at 1.65 GHz over a 16-MHz frequency range (Popov et al. 2002).

There is also another difference between CCFs computed for GPs in our current analysis and ACFs/CCFs calculated for the micropulses (see, e.g., Popov et al. 2002). The parameters of the microstructure are explained by the amplitude-modulated noise (AMN) model, developed by Rickett (1975). The model explains the pulsar microstructure as being an envelope of a complex, white Gaussian noise process. Further elaboration of this model was done by Cordes (1976a) who postulated that the origin of the shot noise is coherent curvature radiation from bunched particles. Cordes (1976b) showed that ACFs/CCFs for micropulses do follow a prediction of the AMN model concerning the amplitude of the microstructure component in the average ACF/CCF. This amplitude is close to 0.5 at zero lag, when properly corrected for the signal-to-noise ratio (S/N) and time smoothing. Thus, even the shortest micropulses do consist of a large number of such shots. However, the CCFs calculated for GPs in our analysis do not obey the prediction of the AMN model, and the correlation coefficients at zero lag are often larger than 0.5, even without a correction for the finite S/N (see figure 8). Therefore, we think that the shortest GP components at 2.2 GHz consist only of a small number of individual shots, or even only of a single elementary shot.

6. Giant Pulses at 600 MHz

Giant pulses appear more often at 600 MHz than at higher frequencies. In more than 5 hr of observations we found 997 GPs with a peak flux density greater than 30 σ — 849 in the main pulse and 148 in the interpulse. The highest peak flux density detected was 2 MJy (1700 σ).

Owing to unusually low scattering (see subsection 6.3), we were able to estimate the width of the pulses, and find the energy distributions separately for pulses of different widths. Below we briefly describe our calculation of energies and widths, and then discuss the results.

6.1. *Data Analysis*

It is well known that GPs from the Crab pulsar occur in two narrow longitude regions, each about 6°.7 wide, namely in the main pulse (MP) and interpulse (IP) regions. Therefore, we analyzed data only from three relatively narrow windows: of the MP and IP windows of 6°.7 width, and of a control noise window (with no pulsar emission) located between the MP and IP windows.

At 600 MHz the search methods differed from those at other frequencies. Instead of selecting pulses stronger than the fixed threshold, we recorded the "width" and "energy" for the point with the maximum flux density in all three windows for every period, regardless of the actual presence of a giant pulse. The properties of the GPs, themselves, were derived from a comparison of the whole sets of "widths" and "energies" on MP/IP windows with those of the noise window. We believe that such method has two main advantages. First, it allows us to neglect any unexpected deviations of noise from a Gaussian. Second, it exempts us from selecting pulses based on their peak flux density, which can be randomly biased by scattering. Considering all this, the analysis can be extended to weaker pulses.

6.1.1. *Calculation of width and energy*

Giant pulses have a complex, jagged form, sometimes with several close components (see figure 9). Here, we considered another technique of GP's width measurements compared with that proposed in subsection 5.1. To find the width of GPs, we used the fact that every giant pulse, regardless of its shape and peak flux density, is, in fact, a region with increased variance of the signal S. Thus, on every MP/IP/noise window we computed a sequence of variances, σ_i^2 over a small floating window,

$$\sigma_i^2 = \sum_{k=1}^{N} (S_{i+k} - \bar{S})^2 \, . \tag{3}$$

The size of the floating window in units of the number of samples, N, was comparable to the typical distance between the components (namely 200 samples, i.e., 25 μs). When such a window covered a GP, the variance rapidly increased. Since the size of the window was about the typical distance between the components of the GP, the rise and decay were smooth, and it was easy to measure the width of such outburst, which we designated as $W_{\sigma_i^2}$. It was measured at a level of 5% of the peak maximum (see figure 9). To obtain the width of GP ($W_{\rm GP}$), we subtracted the size of the window, N, from $W_{\sigma_i^2}$:

$$W_{\rm GP} = W_{\sigma_i^2} - N \, . \tag{4}$$

After that, the data in the MP/IP and noise windows were smoothed with the corresponding value of the widths. The maximum of the smoothed data was regarded as being the total energy, $E_{\rm tot}$, of an event; we obtained $W_{\rm GP}$, which we took to be equal to $W_{\rm e}$. We then converted the derived $W_{\rm e}$, expressed in samples, to microseconds with $\delta t = 0.125\,\mu$s, and we scaled $E_{\rm tot}$ to kJy $\cdot\,\mu$s.

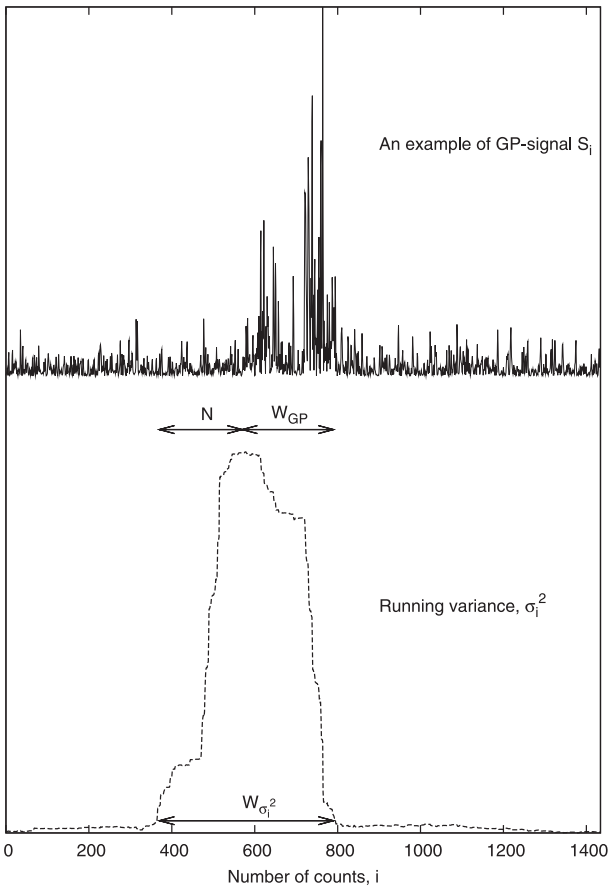

Fig. 9. Example of a single pulse detected at 600 MHz , illustrating the technique of pulse width definition. The solid line represents the pulse intensity, and the dashed line shows the running variance. See text for a more detailed explanation.

As mentioned before, such procedure was performed for every pulsar period in three different longitude windows. In the noise window, $W_{\sigma_i^2}$, was usually less than the size of the floating window, N, resulting in negative "GP" widths. To unify the smoothing procedure, we assigned all such negative widths to the value of 1 sample.

6.2. *GP Widths and Energies*

As can be seen in figure 10, the strongest pulses are, on average, narrow, and their widths are comparable to the scattering width. The dimmer pulses are usually broader. The same tendency was observed at 1.2 GHz (see section 5).

The energy distributions for GPs both from the main pulse and the interpulse are well fitted by a power-law, with the indices depending on the range of widths selected (table 3). However, for MP GPs wider than 8 μs, the energy distribution flattens at low energies (see figure 10), while the energy distribution for IP GPs in the same range of width and energy remains the same. Thus, the cumulative distribution for GPs from the main pulse wider than 8 μs was fitted with 2 power-law functions:

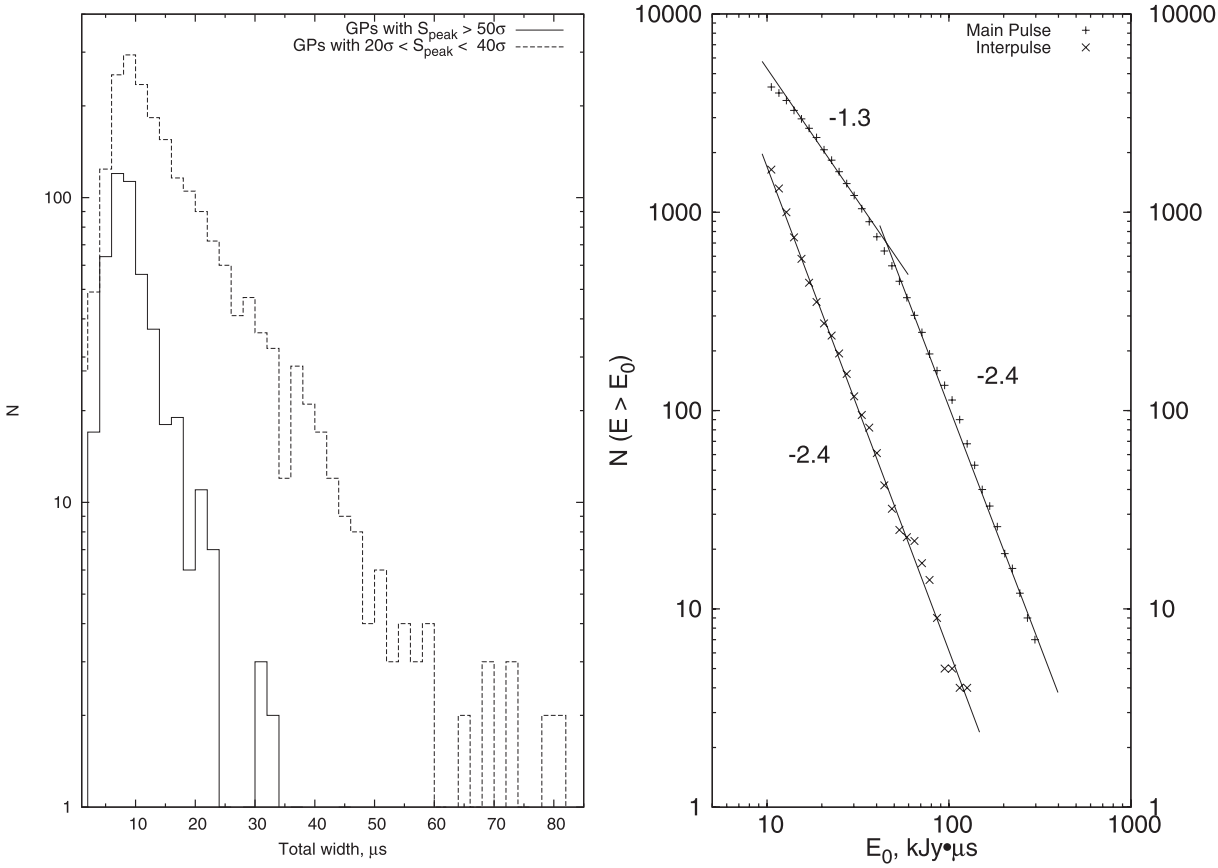

Fig. 10. Histograms of total widths (left), and cumulative energy distribution for GPs with widths of 16–24 μs at 600 MHz (right). The solid line in the histogram represents GPs with peak flux densities of $S_{\rm peak} > 50\sigma$ (the strongest GPs), while the dashed line is for weaker GPs.

Table 3. Power-law indices α of the cumulative energy distributions of GPs at the frequency of 600 MHz for different GP widths.*

Total GP width, μs	Interpulse α	Main Pulse α_1	Main Pulse α_2	$E_{\rm break}$, Jy $\cdot\,\mu$s
<8	-1.5	-1.4		–
8–16	-1.9	-1.2	-1.9	40
16–24	-2.4	-1.3	-2.4	45
>24	-3.2	-1.0	-3.8	55
all	-2.0	-0.9	-2.2	35

* Energies of GPs from the longitude of the main pulse have different power-law distributions for low-energy and high-energy GPs with the clear break energy $E_{\rm break}$ (see text) between them. We list both indices α_1 and α_2 for this case.

$$N(E > E_0) \sim \begin{cases} E_0^{\alpha_1}, \, E_0 < E_{\rm break}, \\ E_0^{\alpha_2}, \, E_0 > E_{\rm break}. \end{cases} \quad (5)$$

Such flattening was previously detected at other frequencies (Bhat et al. 2008; Popov & Stappers 2007 and references therein). The break energy for the overall distribution, 35 kJy $\cdot\,\mu$s, is consistent with the empiric formula for the break energy as a function of the observed frequency, derived by Popov and Stappers (2007),

$$E_{\rm break} \propto 7\nu^{-3.4} \, , \quad (6)$$

where E is in kJy $\cdot\,\mu$s and ν in GHz.

6.3. GP Scattering

At frequencies below $\sim$1 GHz, the pulse shapes are dominated by the scattering broadening, which decreases with increasing frequency for the Crab pulsar as $\tau_{\rm scat} \propto f^{-3.5}$ (Popov et al. 2006a). However, the amount of scattering varies significantly with time. For example, Popov et al. (2006b) found $\tau_{\rm scat}$ to be equal to 45 μs at a frequency of 600 MHz in their observations with the Kalyazin radio telescope in 2003 November. The measured value of $\tau_{\rm scat}$ was estimated by fitting the exponential function $\exp(-t/\tau_{\rm scat})$ to the tail of the average GP profile. In our current observations in 2005 July the scattering broadening was 5–10 times smaller, and to approximate the average GP profile tail we used two exponents with $\tau_{\rm scat}$ values of 4.5 and 17.5 μs, with the short-scale component of the GPs being 4-times larger in amplitude. The mean GP profile was folded by summing 1436 GPs stronger than 50 kJy in peak flux density. They were smoothed by averaging 10 samples (1.25 μs), and aligned by their abrupt leading edges. The tail portion of the average GP profile at 0.6 GHz and its fit are presented in figure 11. A smaller scattering contribution favored our analysis of intrinsic shapes of GPs detected at 2.2 GHz (subsection 5.4).

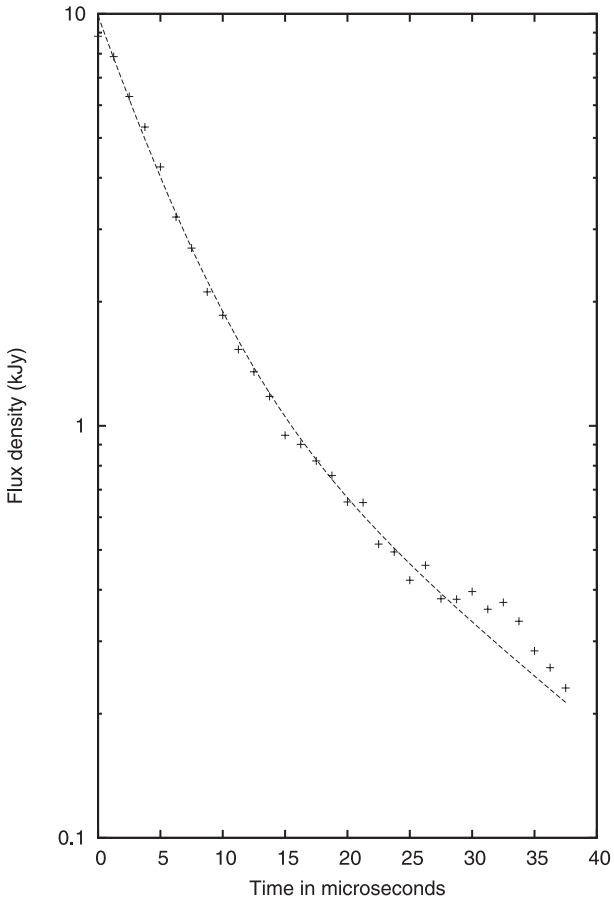

Fig. 11. Tail portion of the average GP profile at 600 MHz folded by summing 1436 GPs stronger than 50 kJy in peak flux density. The dashed line represents the fit by two exponents, $S = 8.1\exp(-t/\tau_{\rm scat,1}) + 1.8\exp(-t/\tau_{\rm scat,2})$, with the scattering times $\tau_{\rm scat,1} = 4.5\,\mu$s and $\tau_{\rm scat,2} = 17.5\,\mu$s.

7. Conclusions

Our study of giant pulses from the Crab pulsar from our simultaneous multifrequency observations with the Kalyazin radio telescope allowed us to draw a number of conclusions about the properties of Crab GPs:

1. Single GPs were often observed simultaneously in the three frequency bands of 0.6, 1.4, and 2.2 GHz, confirming the broad-band nature of the GP emission. The spectral index α has a tendency to flatten towards higher frequencies ($\alpha_{0.6-1.4} = -2.6$ and $\alpha_{1.4-2.2} = -1.8$), as was also reported before by Popov et al. (2008).
2. Instantaneous radio spectra of individual GPs do not follow a single power law in the frequency bands of 0.6, 1.4, and 2.2 GHz. Many GPs observed both at 0.6 and 2.2 GHz were not detected at 1.4 GHz, thus proving a notable spectra modulation at a frequency scale of $\Delta\nu/\nu \approx 0.5$. At a frequency of 1.4 GHz, in addition to diffraction spectra distortions caused by the wave propagation through inhomogeneities of the interstellar plasma, we also distinguished small-scale modulations in radio spectra at a level of $\Delta\nu/\nu \approx 0.01$, intrinsic to the pulsar.
3. GP profiles at the frequency of 2.2 GHz can be presented by unresolved spikes grouped together at a time scale of about 1 μs. These unresolved components are well-correlated over a 60-MHz bandwidth ($\Delta\nu/\nu \approx 0.03$). For a comparison, Hankins (2000) did not find such an correlation for the unresolved structure of GPs between 4535 and 4985 MHz (i.e., $\Delta\nu/\nu \approx 0.1$).
4. Cross-correlation functions of GP profiles in different frequency channels do not obey the prediction of the AMN model (Rickett 1975) for the microstructure of the pulsar radio emission. Thus, unresolved components may represent a small number or even single elementary emitters.
5. The extra non-dispersive time delays of about 0.2 μs found in arrival times of unresolved components of the GP structure at 2.2 GHz are 10-times smaller than the residual dispersion delays of about 2 μs found in TOAs of micropulses for the pulsars B0950+08 and B1133+16 at 1.65 GHz (Popov et al. 2002).
6. The strongest GPs tend to have shorter durations. The same results were reported by Popov and Stappers (2007) and by Bhat et al. (2008) at frequencies of 1.2–1.4 GHz.
7. The distribution of dispersion measures of GPs determined from their TOAs at 0.6 and 1.4 GHz is likely bimodal and can be well-fitted by two Gaussians with mean values of 56.7363 and 56.7373 pc cm^{-3}.
8. The cumulative distribution of GP energies at 600 MHz depends on the effective width of GPs. This distribution obtained only for GPs at the longitude of the main pulse, has a break, and can be represented by two power-law functions with indices of -2.0–-0.9 at high and low energies, respectively. The value of the energy $E_{\rm break}$, where this break occurred, is equal to 35 kJy $\cdot\,\mu$s, which is consistent with the empiric formula $E_{\rm break}$(kJy $\cdot\,\mu$s) $= 7\nu^{-3.4}$ with ν in GHz derived by Popov and Stappers (2007).

References

Bhat, N. D. R., Tingay, S. J., & Knight, H. S. 2008, ApJ, 676, 1200
Bilous, A. V., Kondratiev, V. I., Popov, M. V., & Soglasnov, V. A. 2008, in AIP Conf. Proc., 983, 40 Years of Pulsars: Millisecond Pulsars, Magnetars and More (New York: AIP), 118
Cognard, I., Shrauner, J. A., Taylor, J. H., & Thorsett, S. E. 1996, ApJ, 457, L81
Cordes, J. M. 1976a, ApJ, 210, 780
Cordes, J. M. 1976b, ApJ, 208, 944
Cordes, J. M., Bhat, N. D. R., Hankins, T. H., McLaughlin, M. A., & Kern, J. 2004, ApJ, 612, 375
Cordes, J. M., & Hankins, T. H. 1973, BAAS, 5, 18
Hankins, T. H. 1971, ApJ, 169, 487

Hankins, T. H. 1972, ApJ, 177, L11
Hankins, T. H. 2000, in ASP Conf. Ser., 202, Pulsar Astronomy — 2000 and beyond, ed. M. Kramer, N. Wex, & R. Wielebinski (San Francisco: ASP), 202, 165
Hankins, T. H., & Eilek, J. A. 2007, ApJ, 670, 693
Hankins, T. H., Kern, J. C., Weatherall, J. C., & Eilek, J. A. 2003, Nature, 422, 141
Hankins, T. H., & Rickett, B. J. 1975, in Methods in computational physics (Advances in Research and Applications, Volume 14 — Radio Astronomy), ed. B. Alder, S. Fernbach, & M. Rotenberg (New York: Academic Press), 55
Jenet, F. A., & Anderson, S. B. 1998, PASP, 110, 1467
Jessner, A., Graham, D., Zensus, A., Popov, M. V., Soglasnov, V. A., Kondratiev, V. I., Bilous, A. V., & Moshkina, O. A. 2008, A&A, in preparation
Kinkhabwala, A., & Thorsett, S. E. 2000, ApJ, 535, 365
Knight, H. S. 2006, Chin. J. Astron. Astrophys. Suppl., 6, 41
Kondo, T., Koyama, Y., Nakajima, J., Sekido, M., & Osaki, H. 2003, in ASP Conf. Ser., 306, "New Technologies in VLBI, ed. Y. C. Minh (San Francisco: ASP), 205
Kondratiev, V. I., Popov, M. V., Soglasnov, V. A., Kavalev, Y. Y., Bartel, N., & Ghigo, F. 2007b, in Proc. of the 363 WE-Heraeus Seminar, on Neutron Stars and Pulsars, ed. W. Becker & H. H. Huang, MPE Report 291 (Garching: Max-Plank-Institute für Extraterrestrische Physik), 76
Kondratiev, V. I., Popov, M. V., Soglasnov, V. A., Kovalev, Y. Y., Bartel, N., Cannon, W., & Novikov, A. Yu. 2007a, Astron. Astrophys. Trans., 26, 585
Lorimer, D. R., & Kramer, M. 2004, Handbook of pulsar astronomy (Cambridge: Cambridge University Press)
Lyne, A. G., Pritchard, R. S., & Graham-Smith, F. 1993, MNRAS, 265, 1003
Popov, M. V., et al. 2006a, Astron. Rep., 50, 562
Popov, M. V., et al. 2008, Astron. Rep., 52, 900
Popov, M. V., Bartel, N., Cannon, W. H., Novikov, A. Yu., Kondratiev, V. I., & Altunin, V. I. 2002, A&A, 396, 171
Popov, M. V., Soglasnov, V. A., Kondrat'ev, V. I., & Kostyuk, S. V. 2004, Astron. Lett., 30, 95
Popov, M. V., Soglasnov, V. A., Kondrat'ev, V. I., Kostyuk, S. V., Ilyasov, Yu. P., & Oreshko, V. V. 2006b, Astron. Rep., 50, 55
Popov, M. V., & Stappers, B. 2003, Astron. Rep., 47, 660
Popov, M. V., & Stappers, B. 2007, A&A, 470, 1003
Rickett, B. J. 1975, ApJ, 197, 185
Soglasnov, V. 2007, in Proc. of the 363 WE-Heraeus Seminar on Neutron Stars and Pulsars, ed. W. Becker & H. H. Huang, MPE Report 291 (Garching: Max-Plank-Institut für Extraterrestrische Physik), 68
Soglasnov, V. A., Popov, M. V., Bartel, N., Cannon, W., Novikov, A. Yu., Kondratiev, V. I., & Altunin, V. I. 2004, ApJ, 616, 439